

Moment analysis of focus-diverse point spread functions for modal wavefront sensing of uniformly illuminated circular-pupil systems

Hanshin Lee*

McDonald Observatory, University of Texas at Austin, 1 University Station C1402, Austin, TX, 78712, USA

*Corresponding author: lee@astro.as.utexas.edu

Compiled November 10, 2018

A new concept of using focus-diverse point spread functions (PSFs) for modal wavefront sensing (WFS) is explored. This is based on relatively straightforward image moment analysis of measured PSFs, which differentiates it from other focal-plane wavefront sensing techniques (FPWFS). The presented geometric analysis shows that the image moments are non-linear functions of wave aberration coefficients, but notes that focus-diversity (FD) essentially decouples the coefficients of interest from others, resulting in a set of linear equations whose solution corresponds to modal coefficient estimates. The presented proof-of-concept simulations suggest the potential of the concept in WFS with strongly aberrated high SNR objects in particular.

© 2018 Optical Society of America

OCIS codes: 010.7350,110.2960,080.1010,120.5050,220.4840

Optical wavefront is aberrated during its passage through physical systems due to perturbations like turbulence in Earth atmosphere or misalignment of telescopes. Useful understanding of the observed behaviours of the systems can be obtained by sensing the aberration coefficients of the wavefront. Typically, a wavefront is measured at the pupil of an imaging system, as in Shack-Hartmann sensors (SHS) where wavefront slope is measured and then wave aberration is determined from the measurement [1]. It can be efficient and accurate, but requires a separate relay for pupil re-imaging with additional optical components.

In some cases, one wishes to sense wavefront across the field of view of an instrument by using the built-in components without separate relay components. Such desires can be satisfied by applying FPWFS techniques to focus-diverse images. Curvature sensing (CS) is a FPWFS method where the intensity difference between two extra-focal images are used to determine wavefront [2]. The CS signal is directly related to the shape of a membrane deformable mirror, enabling efficient control of the wavefront compensator [1]. In Phase retrieval, another FPWFS method, wavefront is optimized until its synthetic focus-diverse images closely match the measured ones [3]. It can be accurate and flexible, but may be less efficient than others due to a potentially large number-crunching during optimization. However, progress has been made to address this issue [4–6].

In this Letter, the idea of a new type of FPWFS technique is explored. Like others, it utilizes focus-diverse PSFs, but differs, in that aberrations are sensed via image moment analysis of the PSFs. The presented geometric analysis shows that the moments are non-linear functions of wave aberration coefficients, but notes that FD essentially decouples the coefficients of interest, leading to linear equations whose solution corresponds to modal coefficient estimates. It is argued that this approach has potential in WFS as shown in the presented simulations.

Noll's notations are adopted throughout [7].

Geometrically, aberrated systems spread rays around and blur their PSFs, but the blur shape uniquely differs depending on wave aberrations, e.g. comet-like PSF blur by coma (see pp. 90 in [8] for more examples). Such geometric relations can be explained by the connection between ray and wave aberrations. Suppose that a wavefront Φ on the unit-disk pupil Ω is given as,

$$\Phi = a_1 Z_1 + a_2 Z_2 + a_3 Z_3 + \cdots + a_M Z_M, \quad (1)$$

where a_i are the wave aberration coefficients and Z_i are the Zernike polynomials in the pupil coordinates (x, y) . The ray coordinates (X, Y) at the focus are given by differentiating Φ by x and y , respectively.

$$X = X_0 + 2F \frac{\partial \Phi}{\partial x}, \quad Y = Y_0 + 2F \frac{\partial \Phi}{\partial y}, \quad (2)$$

where (X_0, Y_0) are the ideal image coordinates and F is the focal ratio. The derivative terms are given as,

$$\begin{aligned} 2F \partial \Phi / \partial x &= \vec{a}^T \mathbf{\Gamma}^x \vec{Z} = (\vec{a}'^x)^T \vec{Z} \\ 2F \partial \Phi / \partial y &= \vec{a}^T \mathbf{\Gamma}^y \vec{Z} = (\vec{a}'^y)^T \vec{Z} \end{aligned}, \quad (3)$$

where \vec{a}'^x and \vec{a}'^y are slope coefficient vectors and \vec{Z} is the vector of Z_i . Noll noted the derivatives of Z_i can be given in terms of Z_i through the conversion matrices $\mathbf{\Gamma}^x$ and $\mathbf{\Gamma}^y$ [7]. $a_i'^x$ and $a_i'^y$ are related to a_i , e.g. for $M=10$

$$\begin{aligned} a_1'^x &= 2a_2 + 2\sqrt{2}a_8, & a_1'^y &= 2a_3 + 2\sqrt{2}a_7, \\ a_2'^x &= 2\sqrt{3}a_4 + \sqrt{6}a_6, & a_2'^y &= \sqrt{5}a_5 + \sqrt{10}a_{13}, \\ a_3'^x &= \sqrt{5}a_5 + \sqrt{10}a_{13}, & a_3'^y &= 2\sqrt{3}a_4 - \sqrt{6}a_6 \\ a_4'^x &= 2\sqrt{6}a_8, & a_4'^y &= 2\sqrt{6}a_7, \\ a_5'^x &= 2\sqrt{3}a_7 + 2\sqrt{3}a_9, & a_5'^y &= 2\sqrt{3}a_8 - 2\sqrt{3}a_{10}, \\ a_6'^x &= 2\sqrt{3}a_8 + 2\sqrt{3}a_{10}, & a_6'^y &= -2\sqrt{3}a_7 + 2\sqrt{3}a_9. \end{aligned} \quad (4)$$

One way to quantify the PSF shape is computing its k th moment of order $k = n + m \geq 1$, that is given as,

$$\mu_{nm} = S^{-1} \int_{\Omega} I (X - X_0)^n (Y - Y_0)^m d\Omega, \quad (5)$$

where I is the pupil illumination and S is its integral over Ω . Here, the moment is computed using the pupil plane quantities (i.e. I , X , and Y), whereas this is *usually* done using focal plane quantities. But, note that the focal plane PSF is essentially determined by the pupil plane quantities. Thus, Eq. 5 should lead to the moment as computed in the usual way.

With $I = 1$ over Ω , $S = \pi$ and the centroids become $\mu_{10} = a_1^x$ and $\mu_{01} = a_1^y$. Apparently, μ_{nm} with $k \geq 2$ is non-linear in a_i^x or a_i^y , but only some slope coefficients (say b_i) are coupled to $(a_2^x)^\alpha (a_3^y)^\beta$ where $\alpha + \beta + 1 = k$. Note that a_2^x and a_3^y are the only coefficients affected by defocus (a_4), thus differentiating these with respect to a_4 by $k-1$ times decouples b_i from $(a_2^x)^\alpha (a_3^y)^\beta$. For instance, the derivatives of μ_{nm} at $k=2$ (Eq. 6),

$$\mu_{20} = \sum_{i=2}^M (a_i^x)^2, \mu_{11} = \sum_{i=2}^M a_i^x a_i^y, \mu_{02} = \sum_{i=2}^M (a_i^y)^2, \quad (6)$$

are the followings.

$$\frac{\partial \mu_{20}}{\partial a_4} = 4\sqrt{3}a_2^x, \frac{\partial \mu_{11}}{\partial a_4} = 4\sqrt{3}a_3^x, \frac{\partial \mu_{02}}{\partial a_4} = 4\sqrt{3}a_3^y. \quad (7)$$

Note $a_3^x = a_2^y$ from Eq. 4. Another example is for $k = 3$, where the 2nd partial derivatives of μ_{nm} are given as,

$$\begin{aligned} \frac{\partial^2 \mu_{30}}{\partial a_4^2} &= c(a_4^x + \sqrt{2}a_6^x), \frac{\partial^2 \mu_{12}}{\partial a_4^2} = d(5a_4^x - 3\sqrt{2}a_6^x), \\ \frac{\partial^2 \mu_{03}}{\partial a_4^2} &= c(a_4^y - \sqrt{2}a_6^y), \frac{\partial^2 \mu_{21}}{\partial a_4^2} = d(5a_4^y + 3\sqrt{2}a_6^y), \\ \text{with } a_5^x &= \sqrt{2}a_4^y + a_6^y, a_5^y = \sqrt{2}a_4^x + a_6^x, \end{aligned} \quad (8)$$

where $c = 12\sqrt{3}$ and $d = 4\sqrt{3}$. Solving the above equations produces the slope coefficients. In a similar way, the $k-1$ th partial derivatives of the k th moments can be used to estimate the slope coefficients at the $k-1$ th order. The slope estimates can then be used in Eq. 3 to determine a_i of radial order up to k .

What does it mean to have the derivative of moment in reality then? It is simply *FD*. Through-focusing is one way to achieve it, where the PSF is recorded at N different intra- or extra-focal planes and the image moments of the PSFs are measured. This obviously leads to μ_{nm} that is a function of Δa_4 . Note $N=k$ and $\Delta a_4 = \Delta L / (16\sqrt{3}F^2)$ in the unit of focus perturbation ΔL . Finally, fitting a polynomial of degree $k-1$ to the measured μ_{nm} results in the $k-1$ th coefficient that corresponds to the $k-1$ th derivative of μ_{nm} with respect to a_4 . In summary, one can obtain the dependence of μ_{nm} on a_i^x , a_i^y from Eq. 2, 3, 4 and the $k-1$ th derivative of μ_{nm} with respect to a_4 leads to simple expressions allowing to estimate

a_i . To experimentally measure the derivative, the PSF should be recorded at k different image planes or FDs.

As a proof-of-concept, I demonstrate a simulation where non-zero a_i with $i = 2, 3, 4, \dots, 10$ are estimated by using three through-focus images sampled at -1mm, 0mm, and 1mm ($\Delta a_4 \sim \pm 0.7\lambda$) from the ideal focus of a f/10 system with 2.7m aperture (plate scale $\sim 7.6''/mm$). A standard FFT method was used for synthesising polychromatic PSFs [9].

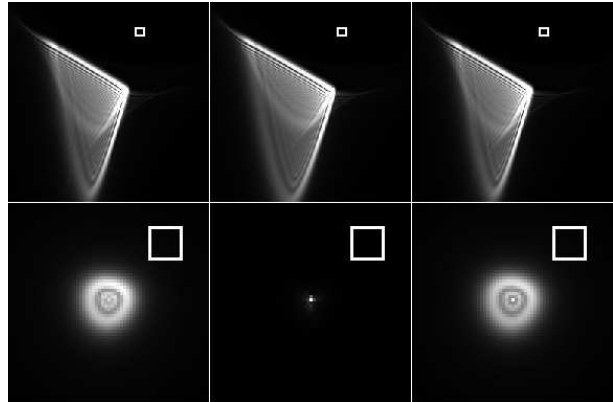


Fig. 1. Polychromatic through-focus PSFs on 512² grid with uniform spectral weight at 11 wavelengths between 514nm and 614nm, Top: Initial, Bottom: After correction, Left: -1mm before focus, Middle: at focus, Right: +1mm after focus. 50 μ m squares overlaid for size comparison. Images in square-root scale.

The initial wavefront error is quite substantial amounting to 5.7λ in rms at $\lambda=514$ nm, making the through-focusing effect in the PSF shape barely noticeable. The pixel size is 5μ m. The estimated coefficients are compared to the input values in Table 1. The estimated slope coefficients (\hat{a}_i^x , \hat{a}_i^y) match the true values (a_i^x , a_i^y) with sub-pixel accuracy. The maximum difference between the estimated (\hat{a}_i) and the true (a_i) wave coefficients is 0.032λ in a_9 . The PSFs after applying \hat{a}_i as corrections are in the bottom row of Figure 1.

Table 1. Slope (in pixel) and wave (in λ) coefficients in Figure 1.

i^k	\hat{a}_i^x	a_i^x	\hat{a}_i^y	a_i^y	\hat{a}_i	a_i
1 ⁰	-11.926	-11.959	-1.078	-1.144	-	-
2 ¹	-27.885	-27.986	7.956	7.968	-1.198	-1.185
3 ¹	7.956	7.968	-30.874	-31.015	1.612	1.636
4 ²	-12.351	-12.505	-13.033	-13.316	-4.241	-4.241
5 ²	1.823	1.766	-18.399	-18.601	1.624	1.626
6 ²	0.932	0.917	20.255	20.598	0.305	0.309
7 ³	-	-	-	-	-1.330	-1.359
8 ³	-	-	-	-	-1.261	-1.276
9 ³	-	-	-	-	1.593	1.614
10 ³	-	-	-	-	1.392	1.408

In the next demonstration, the same images were binned by a factor of 4 (Figure 2). The same moment analysis was applied to the binned images and the resultant wave and slope aberration coefficients are compared to the true values in Table 2. The binning effectively reduces the spatial resolution of the images. This leads to a fewer pixels used in the moment analysis and thus

reduces the moment measurement accuracy. To some extent, binning is equivalent to low-pass filtering, washing out small-scale diffraction structures that may not be accounted for by the geometric wavefront aberrations, although diffraction effect appears to be less of an issue in the current analysis. Overall, the binning impact seems more prominent in the coefficients with odd radial orders ($k=1, 3$) than in the even radial order coefficients ($k=2$). The estimated slope coefficients still approximate the true values with sub-pixel accuracy.

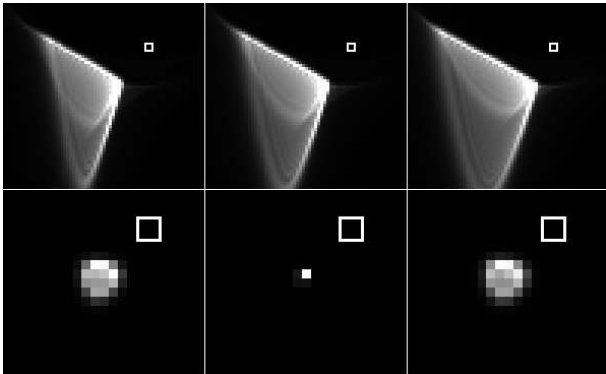


Fig. 2. Polychromatic through-focus PSFs with 4x4 binning, Top: Initial, Bottom: After correction, Left: -1mm before focus, Middle: at focus, Right: +1mm after focus. $50\mu\text{m}$ squares overlaid for comparison. Images in square-root scale.

The maximum difference between \hat{a}_i and a_i is 0.032 wave in a_9 . The through-focus PSFs after applying \hat{a}_i as corrections are shown in the bottom row of Figure 2.

Table 2. Slope (in pixel) and wave (in λ) coefficients in Figure 2.

i^k	\hat{a}'_i^x	a'_i^x	\hat{a}'_i^y	a'_i^y	\hat{a}_i	a_i
1^0	-11.924	-11.959	-1.080	-1.144	-	-
2^1	-27.851	-27.986	7.928	7.968	-1.182	-1.185
3^1	7.928	7.968	-30.884	-31.015	1.607	1.636
4^2	-12.468	-12.505	-13.006	-13.316	-4.239	-4.241
5^2	1.761	1.766	-18.385	-18.601	1.618	1.626
6^2	0.753	0.917	20.155	20.598	0.310	0.309
7^3	-	-	-	-	-1.328	-1.359
8^3	-	-	-	-	-1.273	-1.276
9^3	-	-	-	-	1.582	1.614
10^3	-	-	-	-	1.381	1.408

Finally, random aberrations (from a_2 to a_{15} , i.e. $M=15$) were applied to 21 point objects with different brightness. The aberration, without tip/tilt, amounts to 0.5λ rms at 500nm. The images of four object are shown at the maximum FD of 1λ in the inset (Figure 3). Five FD frames were obtained, where the pixel size is $18\mu\text{m}$ with scale of $0.15''$ at 2.7m aperture and 600nm were used with photon shot noise. The signal-to-noise ratio (SNR), the square root of total photons collected as computed at the zero FD, ranges from 11 to 221. The rms residual error, i.e. the root sum square of $\hat{a}_i - a_i$, is plotted against SNR (blue) with two power-law fits. While the green curve fits the blue data better,

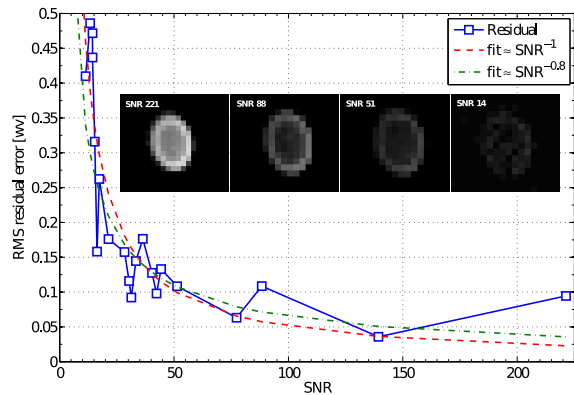


Fig. 3. Four object images at 1λ FD (inset), RMS residual error against SNR for 21 objects.

the red fit also asymptotes the data and follows the general behavior of the accuracy of other WFS techniques ($\sim\text{SNR}^{-1}$) [1]. It appears that SNR higher than 50 per frame is needed to obtain accuracy better than 0.1λ . This translates to $\text{SNR}\sim 20$ for a SHS with $N=30$ sub-apertures, based on the requirement of $2M\leq N$ [11, 12], leading to the theoretical SHS accuracy of 0.05λ [1]. The analysis indicates the proposed technique to be suitable for high SNR cases, while spatial filtering, noise reduction, or thresh-holding could help improve its robustness in low SNR cases.

The demonstrations suggest the feasibility of the proposed geometric concept in WFS with high SNR and strong aberrations in particular. The fact that the moment analysis is just an extension of the routine computation of image centroid or full-width-half-maximum can make all appropriate objects recorded in an image frame be potential WFS targets. This can certainly permit a straightforward and rapid WFS potentially over a wide field of view, which can be particularly attractive in active diagnosis of alignment-driven field aberrations of imaging systems [13] or wide-field adaptive image compensation. The error propagation is to be separately discussed with other considerations including aberration aliasing, diffraction, and FD implementation.

References

1. J. W. Hardy, *Adaptive Optics for Astronomical Telescopes*, (Oxford, 1998).
2. F. Roddier, "Wavefront sensing and the irradiance transport equation," *Appl. Opt.*, **29**, 1402 (1990).
3. J. R. Finey, "Phase-retrieval algorithm: a comparison," *Appl. Opt.*, **21**, 2758 (1982).
4. J. Dolne, P. Menicucci, D. Miccolis, K. Widen, H. Seiden, F. Vachss, and H. Schall, "Advanced image processing and wavefront sensing with real-time phase diversity," *Appl. Opt.*, **48**, A30-A34 (2009).
5. R. Gonsalves, "Small-phase solution to the phase-retrieval problem," *Opt. Lett.*, **26**, 684-685 (2001).
6. S. Meimon, T. Fusco, and L. Mugnier, "LIFT: a focal-plane wavefront sensor for real-time low-order sensing

- on faint sources,” *Opt. Lett.* **35**, 3036-3038 (2010).
7. R.J. Noll, “Zernike polynomials and atmospheric turbulence,” *J. Opt. Soc. Am.*, **66**, 207 (1976).
 8. V.N. Mahajan, *Aberration Theory Made Simple*, (SPIE, 1991).
 9. J. W. Goodman, *Introduction to Fourier Optics*, 3rd ed. (Roberts & Company, 2005).
 10. N. Roddier, “Atmospheric wavefront simulation using Zernike polynomials,” *Opt. Eng.* **29**, 1174 (1990).
 11. J.Y.Wang and D.E.Silva, ”Wave-front interpretation with Zernike polynomials,” *Appl. Opt.* , **19**, 1510 (1980).
 12. M.G. Lofdahl, A.L. Duncan, and G.B.Scharmer, ”Fast Phase Diversity Wavefront Sensing for Mirror Control,” *Proc. SPIE* **3353**, 952 (1998).
 13. H. Lee, “Optimal collimation of misaligned optical systems by centering primary field aberrations,” *Opt. Express* **18**, 19249 (2010).